Journal of Catalysis 273 (2010) 50–58

Contents lists available at ScienceDirect

Journal of Catalysis

journal homepage: www.elsevier.com/locate/jcat

Selectivity loss of Pt/CeO_2 PROX catalysts at low CO concentrations: mechanism and active site study

Christopher S. Polster [a], Rong Zhang [a], Michael T. Cyb [a], Jeffrey T. Miller [b], Chelsey D. Baertsch [a,*]

[a] School of Chemical Engineering, Purdue University, 480 Stadium Mall Drive, West Lafayette, IN 47907, USA
[b] Argonne National Laboratory, CSE, 9700 S. Cass Ave., Argonne, IL 60439, USA

ARTICLE INFO

Article history:
Received 23 December 2009
Revised 27 April 2010
Accepted 28 April 2010

Keywords:
Platinum
Ceria
Pt/CeO_2
PROX
Active site density
Anaerobic reaction
Anaerobic titration
CO oxidation
H_2 oxidation
Redox mechanism

ABSTRACT

CO and H_2 oxidation were studied over a series of Pt/CeO_2 catalysts with differing Pt loadings and dispersions. Kinetic rate analysis confirms the presence of dual Langmuir–Hinshelwood (L–H) and Mars and van Krevelen (M–vK) pathways and is used to explain the loss in CO oxidation selectivity at low CO concentrations. *In situ* diffuse reflectance infrared Fourier transform spectroscopy (DRIFTS) shows the strong CO coverage dependence on both CO and O_2 concentrations and explains the transition from L–H to M–vK reaction character. Redox site measurements are performed on Pt/CeO_2 catalysts by anaerobic titrations under conditions where the M–vK pathway dominates the reaction rate. Similar redox site densities per interfacial Pt atom suggest that interfacial Pt–O–Ce sites are responsible for M–vK redox activity.

1. Introduction

A wide variety of catalysts are used for the preferential oxidation (PROX) of CO in excess H_2. Among these catalysts include both supported noble metals such as Au/CeO_2 [1–3], Pt/CeO_2 [4–6], Pt/Al_2O_3 [7,8], Rh/CeO_2 [9,10], $Pt–Ru/SiO_2$ [11] and mixed transition metal oxides such as $CuO_x–CeO_2$ [12–18]. Common supports for noble metal PROX catalysts can be classified as redox (such as CeO_2), acidic (such as Al_2O_3) or relatively inert (such as SiO_2) in nature [19], while most metal oxide catalysts (regardless of composition) tend to contain mostly redox character [17,20,21]. CO oxidation on Pt has been shown to follow a Langmuir–Hinshelwood mechanism [5,6,22] and when supported by Al_2O_3, alternate pathways for H_2 oxidation (spillover to the support) lead to losses in selectivity during PROX [7]. In contrast, mechanisms for CO and H_2 oxidation on metal oxide catalysts like $CuO_x–CeO_2$ are typically described by Mars and van Krevelen reaction mechanisms [13,17]. Noble metal catalysts on redox supports display both Langmuir–Hinshelwood and Mars and van Krevelen kinetics where presumably the reaction pathways take place both directly on the metal sites and at redox sites at the interface of metal particles [9,10,23]. The purpose of this work is to elaborate on the details and conditions leading to this parallel reaction pathway model for Pt/CeO_2 catalysts, explain reasons for selectivity losses at low CO pressures in comparison with other PROX catalysts and quantify redox sites to confirm the requirement of interfacial Pt–O–Ce sites for redox activity.

2. Experimental methods

2.1. Catalyst synthesis

Four Pt/CeO_2 catalysts were prepared using different CeO_2 supports, preparation methods and Pt loadings. Preparation methods for each catalyst are described below, with each catalyst name represented as x.xx Pt/CeO_2 (x.xx refers to Pt wt%).

2.1.1. Catalyst 1 – 0.43 Pt/CeO_2

The CeO_2 support was prepared by the urea gelation technique [14]. Two solutions were prepared including a precursor solution of $(NH_4)_2Ce(NO_3)_6$ (Alfa Aesar, 99.5%) dissolved in 135 mL deionized water to a concentration of 0.5 M and a 7.5 M urea solution (Alfa Aesar, 99.5%) one-third the volume of the precursor solution. Both solutions were heated to near their boiling points, and the urea solution was added steadily by buret to the precursor solution

* Corresponding author. Fax: +1 765 494 0805.
E-mail address: baertsch@purdue.edu (C.D. Baertsch).

0021-9517/$ - see front matter © 2010 Elsevier Inc. All rights reserved.
doi:10.1016/j.jcat.2010.04.017

over a period of 10 min (total of 45.5 mL) while stirring. The solution was then stirred and boiled gently (around 373 K) for 2 h during which the solution becomes a gel and changes color from bright orange to tan, after which it is aged for another 2.5 h at approximately 415 K. The aged material was washed twice by stirring vigorously in hot deionized water for 30 min and then vacuum filtered. The support was dried overnight in an oven at 383 K and calcined in dry air at 923 K for 4 h resulting in CeO2 with a BET surface area of 16.0 $m^2 g^{-1}$. Pt was introduced by a modified reduction–deposition technique [4]. A solution of 53 mg chloroplatinic acid hexahydrate (Sigma–Aldrich, ACS reagent) in 80 mL of deionized water was used to suspend the CeO_2 support (~2 g). A 1 M solution of NaOH (Mallinckrodt, ACS reagent) was added drop-wise to the solution while it was heated to 338 K and stirred. Once the pH of the solution reached ~12, 80 μL of 37% formaldehyde (Sigma–Aldrich, ACS reagent) was added. The solution was allowed to age for 1 h while maintaining a temperature of 338 K. The solid left behind was washed and filtered until no residual chloride remained in the filtrate, determined by silver nitrate addition. The catalyst was then dried overnight at 383 K and calcined in dry, flowing air for 4 h at 473 K.

2.1.2. Catalyst 2 – 0.41 Pt/CeO_2

The remainder of the catalysts was prepared by supporting Pt on CeO_2 made by treating 500 g of cerium (III) acetate hydrate at 698 K in air for 24 h yielding CeO_2 with a BET surface area of 80 $m^2 g^{-1}$. For the 0.41 Pt/CeO_2 catalyst, a slurry containing 11.0 g of CeO_2 in 200 mL H_2O and 5 mL concentrated NH_4OH (pH ~10.5) was combined with a solution containing 0.66 g $Pt(NH_3)_4(NO_3)_2$ in 50 mL H_2O and 2 mL concentrated NH_4OH. The Pt solution was added to the CeO_2 slurry and stirred for 30 min, filtered, washed twice with 200 mL cold H_2O and dried at 373 K. The catalyst was calcined in flowing air at 498 K for 3 h.

2.1.3. Catalyst 3 – 1.04 Pt/CeO_2

The 1.04 Pt/CeO_2 catalyst was prepared by wet impregnation. A solution 0.3 g of $Pt(NH_3)_4(NO_3)_2$ dissolved in 5 mL of deionized water was added to 10.0 g of CeO_2. The catalyst was dried at 373 K and calcined in dry air at 498 K.

2.1.4. Catalyst 4 – 2.78 Pt/CeO_2

The 2.78 Pt/CeO_2 catalyst was prepared by wet impregnation. A solution of 0.66 g $Pt(NH_3)_4(NO_3)_2$ in 5.5 mL H_2O was added to 11.0 g CeO_2, then dried at 373 K and calcined in flowing air at 498 K for 3 h.

2.2. Catalyst characterization

The 0.43 Pt/CeO_2 catalyst was characterized by atomic absorption spectroscopy (AAS) to determine Pt weight loading. AAS measurements were made with a Perkin-Elmer AAnalyst 300 spectrometer using an air-acetylene flame. The sample for AAS measurement was made by dissolving the catalyst in concentrated HNO_3:HCl:HF mixtures (4:4:1) at room temperature and then diluting in DI water. Pt standards of ~1, ~5 and ~10 mg/L were prepared by dissolving chloroplatinic acid hexahydrate in deionized water to the appropriate proportions. Weight percentages were obtained from concentration measurements at wavelength 265.9 nm with a slit width of slit 0.7 nm. For the Pt/CeO_2 samples with 0.41, 1.04 and 2.78 wt% Pt, weight percentages were determined by inductively coupled plasma atomic emission spectrometry (ICP-AES). Specific surface areas for all samples in this study were determined by nitrogen physisorption (BET method) using a Micromeritics ASAP 2000 porosimeter.

For all catalysts, Pt dispersion was determined from average Pt–Pt coordination using X-ray absorption spectroscopy (XAS). X-ray absorption spectra were measured at the 10-ID beam line of the Materials Research Collaborative Access Team (MRCAT) at the Advanced Photon Source, Argonne National Laboratory. A double-crystal Si(1 1 1) monochromator was used in conjunction with an uncoated glass mirror to minimize the presence of harmonics. Ionization chambers were optimized for the maximum current with linear response (ca. 10^{10} photons detected s^{-1}) using a mixture of N_2 and He in the incident X-ray detector and a mixture of ca. 20% Ar in N_2 in the transmission and fluorescence X-ray detectors. The measurements were taken using fluorescence detection during continuous scanning from 11,300 eV to 12,489 eV, and an average of 9 spectra were used to minimize noise. A Pt foil spectrum was acquired simultaneously with each measurement for energy calibration at the Pt L3 edge. About 0.5 g of the catalyst sample was pressed into a tilted (45°) self-supporting wafer in a cylindrical holder for fluorescence measurement. The sample was dried in He (180 sccm, with O_2 trap) while ramping up the temperature to 473 K and subsequently reduced at 523 K for 30 min in flowing 4% H_2 (200 sccm). Then the sample was purged in He for 5 min to remove adsorbed H_2 and cooled under flowing He (180 sccm) to room temperature. The X-ray absorption spectra were collected in a static hydrogen atmosphere at room temperature. EXAFS data analysis was carried out with WinXAS 3.1 software. Standard procedures were used for background correction and normalization. The reference data of phase shifts and backscattering amplitudes of the Pt–Pt pair were obtained from Pt foil. The Pt–Pt coordination numbers were obtained by a least square fit in *r*-space of the isolated multiple shell with a *k*-weighting of 2.

2.3. Reaction characterization

CO preferential oxidation (PROX) performance of 0.43 Pt/CeO_2 was evaluated at CO/H_2 ratios typical of water–gas shift reactor effluent [24–26] (50% H_2, 1% CO, 0.5% O_2, balance He) over a temperature range of 283–383 K. Kinetics of CO and H_2 oxidation at a broad range of CO and H_2 concentrations were studied at 333 K. CO concentrations ranged from 10 ppm to 1%, H_2 concentrations ranged from 5% to 85%, and O_2 concentrations ranged from 10 ppm to 1%. Catalyst powders (particle sizes 75–125 μm) were supported on a quartz frit in a vertical U-shaped quartz reactor (I.D. 10 mm). Temperature measurement and control was performed with a thermocouple resting in a well in contact with the catalyst bed. Reactor effluent was analyzed using an Agilent MicroGC 3000, with a lower detection limit on water of approximately 2 ppm. Fractional conversions for both CO and H_2 were calculated by disappearance, as shown in (1), where $P_{CO,out}$ is the CO partial pressure in the product mixture under reaction conditions and $P_{CO,in}$ is the CO partial pressure in the reaction feed. Reaction selectivity was calculated by product formation, shown by (2), where $P_{CO_2,out}$ and $P_{H_2O,out}$ are CO_2 and H_2O partial pressures under reaction conditions. No other products were observed at any tested reaction conditions.

$$X_{CO} = 1 - P_{CO,out}/P_{CO,in} \quad (1)$$

$$S_{CO_2} = P_{CO_2,out}/(P_{CO_2,out} + P_{H_2O,out}) \times 100\% \quad (2)$$

All rate measurements were made after first treating the catalyst in 2% CO balance He for 2 h at 473 K, then cooling to reaction temperature. Data that are reported specifically as oxidation rates are collected under conditions where the limiting reagent (either CO or O_2) conversion is less than 10%, such that the reactor can be considered differential. Rates are neither dependent on gas flow rate nor particle size, ruling out the existence of either internal or external mass transfer limitations at the conditions used in this study. The amount of water formed during reactions is well below the relative saturation pressure of H_2O at 333 K in catalyst pores as

Table 1
Summary of Pt/CeO_2 structure characteristics. Catalyst name is x.xx Pt/CeO_2, where x.xx is the Pt loading in wt%. Pt dispersion is determined using a correlation relating XAS coordination number and dispersion from H_2 chemisorption as presented in Ref. [29].

Catalyst name	BET surface area ($m^2\,g^{-1}$)	CeO_2 crystallite size (nm)	Average Pt–Pt coordination number from XAS	Pt dispersion* (%)
0.43 Pt/CeO_2	4.0	29.1	6.0	61
0.41 Pt/CeO_2	77.8	14.6	5.0	83
1.04 Pt/CeO_2	66.0	14.5	5.2	78
2.78 Pt/CeO_2	78.1	14.3	6.0	61

small as 2 nm, as confirmed using the Kelvin equation. The mean pore diameter of catalysts used in this study range from approximately 6 to 12 nm as determined from N_2 physisorption at 77 K.

Statistical analysis of the rate data was done by several techniques. In order to determine statistical significance of parameter variation, single factor ANOVA (analysis of variance) tests were performed on some data sets by comparing the ratio of "between group" variance with "within group" variance. The ratio of the two variances follows an *F*-distribution, where a ratio higher than some critical value (determined by degrees of freedom and degree of confidence) confirms statistical significance of the varied parameter. All regressed slopes of data are reported with an error of twice the standard error of the point estimate for the slope, representing roughly a 95% confidence interval. Error bars for any single point data are represented by some multiple of the standard deviation of the data within the set, as noted.

Anaerobic titration techniques (detailed in [27]) were used to quantify redox site densities. In this method, O_2 was instantaneously removed from a steady-state oxidation process and replaced with a make-up flow of He using a 4-port zero dead volume Valco switching valve. The reactor system reached zero O_2 concentration within 4 s of the switch time for all experiments in this study, as verified by monitoring $m/z = 32$ using a Hiden HPR 20 Gas Analyzer. Anaerobic titrations were performed using CO as the probe molecule. Product formation rates during anaerobic titration were measured by mass spectrometry by monitoring $m/z = 44$ for CO_2.

2.4. In situ DRIFTS measurements

In situ diffuse reflectance infrared Fourier transform spectroscopy (DRIFTS) data was collected with a Nicolet Magna-860 spectrometer using a Harrick Scientific Praying Mantis diffuse reflectance accessory (DRA) and *in situ* reaction cell (HVC-DRP). Spectra were averaged over 128 scans with a resolution of $4\,cm^{-1}$ and mirror velocity of $1.8988\,cm\,s^{-1}$. Approximately 30 mg of powdered catalyst was loaded into the reaction cell and supported on a horizontal quartz frit. Gases were mixed upstream by Tylan mass flow controllers and passed downward through the catalyst bed. Temperature is measured and controlled by a thermocouple immediately beneath the catalyst bed. The infrared beam was focused onto the catalyst surface prior to enclosing the catalyst in a dome fitted with ZnS windows. A background spectrum was collected at reaction temperature after exposure to an O_2/He mixture for 30 min. This background spectrum was used to convert reflectance measurements into absorbance units. DRIFTS was used in this study to monitor CO coverage in different CO/O_2 mixtures at 333 K.

3. Results and discussion

3.1. Catalyst characterization

Table 1 summarizes the surface area, CeO_2 crystallite size, Pt–Pt coordination number obtained from fitting the FT magnitude of the Pt L3 EXAFS (as shown in Fig. 1) and correlating Pt dispersion of the four investigated Pt/CeO_2 catalysts. A wide variety of characterized Pt/CeO_2 catalysts were available for kinetic testing; however, these four catalysts were specifically chosen for comparison as they have similar dispersion, yet different weight loading, thus providing a series of catalysts containing a range of Pt–CeO_2 interfacial areas over which to compare with redox site density.

The catalysts 0.41 Pt/CeO_2, 1.04 Pt/CeO_2 and 2.78 Pt/CeO_2 contain common CeO_2 supports, reflected by their similar CeO_2 crystallite sizes of 14.6, 14.5 and 14.3 nm, respectively, determined from XRD. The fourth catalyst, 0.43 Pt/CeO_2, contains a support that was calcined at higher temperature (923 K versus 698 K) and is considerably more crystalline with a crystallite size of 29.1 nm.

3.2. Catalyst performance and selectivity comparison

An important aim of this work is to understand the mechanisms for selectivity loss of Pt/CeO_2 catalysts for PROX at low CO concentrations. Thus, it is useful to compare the CO preferential oxidation performance of 0.43 Pt/CeO_2 with other PROX catalysts that show high activity and selectivity. Fig. 2 displays 0.43 Pt/CeO_2 selectivity and conversion as a function of temperature (283–383 K) for a gas mixture of 50% H_2, 1% CO, 0.5% O_2, balance He. The catalyst 0.43 Pt/CeO_2 exhibits nearly 100% CO oxidation selectivity at all temperatures below 333 K with 1% CO in the reaction feed. However, at higher temperatures (343–383 K), Pt/CeO_2 does not reach high CO conversions without a substantial loss in selectivity, unlike other PROX catalysts such as CuO_x–CeO_2 [12,16] and Au/CeO_2 [1].

In addition to PROX applications, highly selective CO oxidation catalysts are desirable for use as catalytic substrates in micro-calorimetric CO detectors for H_2 fuel cells, a technology described in previous work [16]. The key for operating such a sensor is maintaining nearly 100% catalytic CO oxidation selectivity at very low CO concentrations, since the application requires detection of

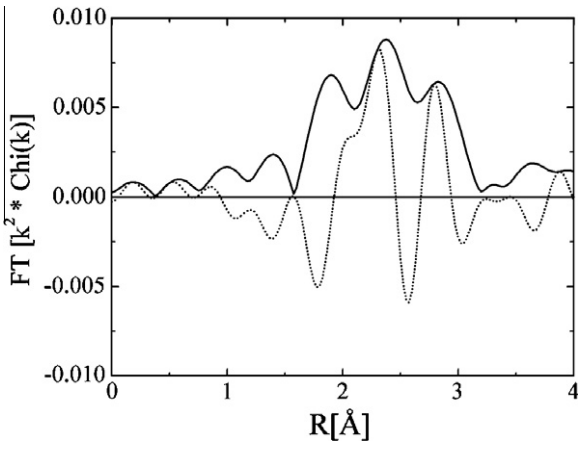

Fig. 1. k^2-Weighted magnitude of the XAS Fourier transform of 2.78 wt% Pt/CeO_2 (bold line: real component of the FT magnitude, thin line: imaginary component of the FT magnitude).

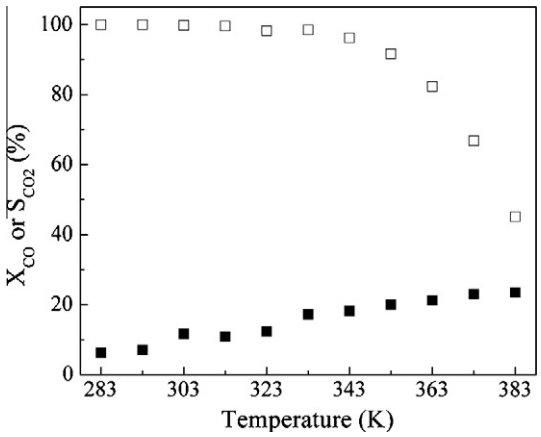

Fig. 2. PROX performance of 0.43 Pt/CeO_2. Closed squares represent CO conversion and open squares represent CO_2 selectivity. Reaction conditions: 50% H_2, 1% CO, 0.5% O_2, balance He. Catalyst weight = 100 mg, flow rate = 100 sccm.

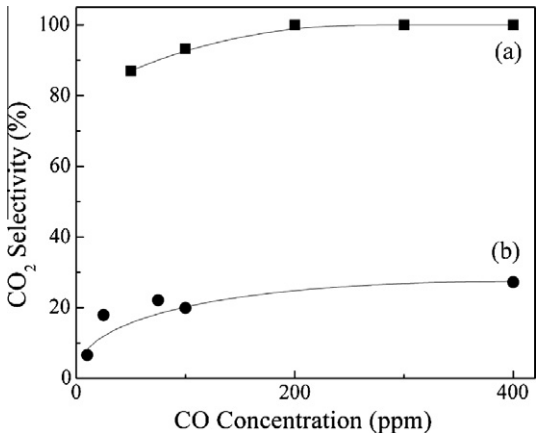

Fig. 3. Comparison of catalyst selectivity as a function of CO concentration in excess H_2 at 333 K. (a) CuO_x–CeO_2 [16] and (b) 0.43 Pt/CeO_2.

low levels of CO (10–100 ppm) with very little false positive response from H_2 [5]. Fig. 3 shows the selectivity at 333 K of 0.43 Pt/CeO_2 and CuO_x–CeO_2 [16] as a function of CO concentration. In comparison with CuO_x–CeO_2, which maintains high CO oxidation selectivity over a wide range of low CO pressures, selectivity drops to around 20% or lower over Pt/CeO_2 in the range that CO must be detected (<100 ppm), indicating that this catalyst is not an adequate substrate for such a sensor application. An explanation of the selectivity loss exhibited by 0.43 Pt/CeO_2 requires more detailed understanding of the underlying CO and H_2 oxidation mechanisms.

3.3. Proposed mechanism

CO and H_2 oxidation have previously been proposed to follow both Langmuir–Hinshelwood and Mars and van Krevelen pathways over supported noble metal catalysts, generally as a function of CO pressure [9,10]. Shown below is the proposed mechanism in detail, which describes this dual pathway, where M is a Pt site, O^* is a support lattice oxygen, and □ is a lattice vacancy. Steps (3)–(9) describe the Langmuir–Hinshelwood (L–H) pathway and have been proposed and justified in another work on Pt/Al_2O_3 catalysts [7]. Step (10) is spillover from the Pt particle to the support to form hydroxyl groups on support lattice oxygen. Steps (11) and (12) are the rate-determining steps for the Mars and van Krevelen (M–vK) pathway for H_2 and CO oxidation, respectively. Also, step (13) is the reoxidation of the lattice vacancies by gas-phase oxygen. The specific mechanism of this reoxidation is not discussed here, but work on the kinetics of this step has been done on supported VO_x catalysts and can be found elsewhere [28].

$$CO + M \leftrightarrow M{-}CO \quad K_1 \tag{3}$$
$$O_2 + M \leftrightarrow M{-}O_2 \quad K_2 \tag{4}$$
$$M{-}O_2 + M \rightarrow 2M{-}O \quad k_3 \tag{5}$$
$$M{-}CO + M{-}O \rightarrow CO_2(g) + 2M \quad k_4 \tag{6}$$
$$H_2 + 2M \leftrightarrow 2M{-}H \quad K_5 \tag{7}$$
$$M{-}H + M{-}O \rightarrow M{-}OH + M \quad k_6 \tag{8}$$
$$M{-}OH + M{-}H \rightarrow H_2O(g) + 2M \quad k_7 \tag{9}$$
$$M{-}H + O^* \leftrightarrow O^*{-}H + M \quad K_8 \tag{10}$$
$$M{-}H + O^*{-}H \rightarrow H_2O(g) + M + \square \quad k_9 \tag{11}$$
$$M{-}CO + O^* \rightarrow CO_2(g) + M + \square \quad k_{10} \tag{12}$$
$$O_2 + 2\square \leftrightarrow 2O^* \quad K_{11} \tag{13}$$

Since parallel oxidation pathways are being considered, two rate-determining steps (one for the L–H model and one for the M–vK model) can be written for both CO and H_2 oxidation. Resulting oxidation rates for both CO and H_2 are shown in Eqs. (14)–(17), where z is the coordination number between the two sites used, and [L] is site density such that $z/[L]$ (or $z'/[L]$) is an effective probability of the sites being in contact. Site balances can be written for both Pt sites (all M–X species) and the lattice sites (hydroxyls, lattice oxygen and vacancies), yielding Eqs. (18)–(21) as the rigorous rate expressions. Eqs. (18) and (19) are individual rate expressions for L–H and M–vK CO oxidation pathways, respectively, while Eqs. (20) and (21) are the same expressions for H_2 oxidation. Due to the parallel nature of the oxidation pathways, each rate can be expressed by the sum of the L–H and M–vK rates.

$$r_{CO}^{L-H} = k_4[M{-}CO][M{-}O]\frac{z}{[L]} \tag{14}$$

$$r_{CO}^{M-vK} = k_{10}[M{-}CO][O^*]\frac{z'}{[L]} \tag{15}$$

$$r_{H_2}^{L-H} = k_7[M{-}H][M{-}OH]\frac{z}{[L]} \tag{16}$$

$$r_{H_2}^{M-vK} = k_9[M{-}H][O^*{-}H]\frac{z^*}{[L]} \tag{17}$$

$$r_{CO}^{L-H} = \frac{2zk_3k_4K_1K_2[CO][O_2][L]}{(k_4K_1[CO]+k_6\sqrt{K_5[H_2]})\left[1+K_1[CO]+\sqrt{K_5[H_2]}+K_2[O_2]+\left(1+\frac{k_6}{k_7}\right)\frac{2k_3K_2[O_2]}{k_4K_1[CO]+k_6\sqrt{K_5[H_2]}}\right]^2} \tag{18}$$

$$r_{CO}^{M-vK} = \frac{z'k_{10}K_1\sqrt{K_{11}[O_2]}[CO][L][O^*]_T}{\left[1+K_1[CO]+\sqrt{K_5[H_2]}+K_2[O_2]+(1+\frac{k_6}{k_7})\frac{2k_3K_2[O_2]}{k_4K_1[CO]+k_6\sqrt{K_5[H_2]}}\right](1+\sqrt{K_{11}[O_2]}+K_8\sqrt{K_5K_{11}[O_2][H_2]})} \tag{19}$$

$$r_{H_2}^{L-H} = \frac{2zk_3k_6K_2\sqrt{K_5[H_2]}[O_2][L]}{(k_4K_1[CO]+k_6\sqrt{K_5[H_2]})\left[1+K_1[CO]\sqrt{K_5[H_2]}+K_2[O_2]+\left(1+\frac{k_6}{k_7}\right)\frac{2k_3K_2[O_2]}{k_4K_1[CO]+k_6\sqrt{K_5[H_2]}}\right]^2} \tag{20}$$

$$r_{H_2}^{M-vK} = \frac{z'k_9K_5K_8\sqrt{K_{11}[O_2]}[H_2][L][O^*]_T}{\left[1+K_1[CO]+\sqrt{K_5[H_2]}+K_2[O_2]+\left(1+\frac{k_6}{k_7}\right)\frac{2k_3K_2[O_2]}{k_4K_1[CO]+k_6\sqrt{K_5[H_2]}}\right](1+\sqrt{K_{11}[O_2]}+K_8\sqrt{K_5K_{11}[O_2][H_2]})} \tag{21}$$

It is apparent therefore that CO and H_2 oxidation rates have very complex dependences on reactant concentrations, with many rate and equilibrium constants, making it particularly difficult to dis-

criminate between models of this complexity. Thus, the aim of this work is to qualitatively show that both pathways are evident and use that to describe losses in PROX selectivity at low CO concentrations.

3.4. Kinetic analysis

Kinetic studies of PROX reactions over Pt/Al_2O_3 [7] have been described using only the L–H pathway and the assumption that nearly all adsorption sites are occupied by CO ($[L] \sim [M–CO]$), yielding Eqs. (22) and (23). It is noticeable by these expressions that the rates of CO and H_2 oxidation are both strongly inhibited by the presence of CO. Both of these equations are bound by the assumption that the surface is mostly dominated by CO, which is true under most PROX reaction conditions using a 1% CO reactant feed [6]. However, at low CO concentrations, typical L–H behavior should be observed with a CO order between 0 and 1.

$$r_{CO} = \frac{2zk_3k_4K_2[O_2][L]}{K_1[CO](k_4K_1[CO] + k_6\sqrt{K_5[H_2]})} \tag{22}$$

$$r_{H_2} = \frac{2zk_3k_6K_2\sqrt{K_5[H_2]}[O_2][L]}{(K_1[CO])^2(k_4K_1[CO] + k_6\sqrt{K_5[H_2]})} \tag{23}$$

Fig. 4a is a log–log plot of CO oxidation rate as a function of CO concentration (10–100 ppm CO) during PROX experiments (50% H_2, 0.5% O_2) at 333 K on 0.43 Pt/CeO_2. From 10 to 50 ppm CO, positive CO order is observed (0.46), implying that at these CO concentrations CO coverage on the Pt particles is fractionally low. From 50 to 100 ppm CO, an inhibition effect is observed (order ~ -1), which can be interpreted as CO coverage reaching saturation ($[M–CO] \rightarrow [L]$) and Eq. (22) becomes an appropriate governing equation in these conditions. The corresponding H_2 oxidation rates are shown in Fig. 4b and exhibit the same characteristics. Much like the CO rate, the H_2 rate exhibits a transition to more CO inhibited behavior around 50 ppm CO. According to Eq. (23), a strong CO order (-2 to -3) is expected in this regime. The data suggests an even stronger CO inhibition (-4.6), but there is large error on this value due to the highly sensitive H_2 rate dependence on CO concentration in this regime. Single factor ANOVA tests (F-test, $f_{5,25} = 3.85$ at 99% significance level) of data sets collected with replicates (with averages and corresponding confidence intervals on the mean shown in Fig. 4) were performed to validate the observed trends. The statistical test shows that the CO and H_2 rates vary significantly with CO concentration, with F ratios of 8.2 (CO oxidation rates) and 108.7 (H_2 oxidation rates). Further, two separate regimes can be confirmed by error values reported for the slopes of trends from 0 to 50 ppm CO and 50 to 100 ppm CO, which are given as twice the standard error (~95% confidence) on the point estimate for the slope. All together, Fig. 4 indicates that under these conditions (25% H_2, 0.5% O_2, 10–100 ppm CO), CO and H_2 oxidation pathways dominantly follow a Langmuir–Hinshelwood model. Also, due to the low CO coverage ($[M–CO] \ll [L]$), H_2 oxidation is very high, and selectivity is correspondingly low, especially below 50 ppm CO (Fig. 3).

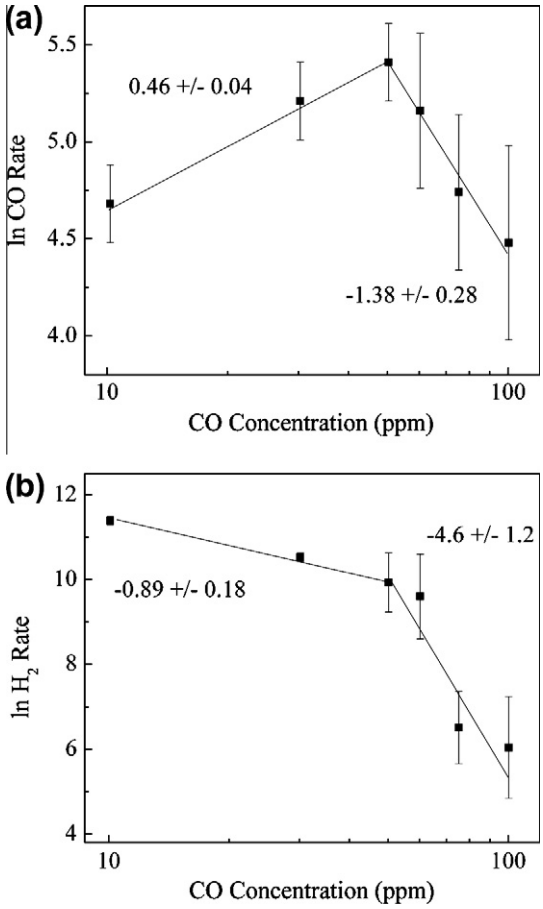

Fig. 4. Log–log plot of (a) CO oxidation rate and (b) H_2 oxidation rate as a function of CO concentration. Corresponding rates are given as 10^{-9} mol g^{-1} s^{-1}. Rates are normalized by a factor of conditions: 25% H_2, 0.5% O_2, bal He, T = 333 K. Error bars represent +/− one standard deviation. Error is estimated from at least 3 and up to 7 experiments at each concentration.

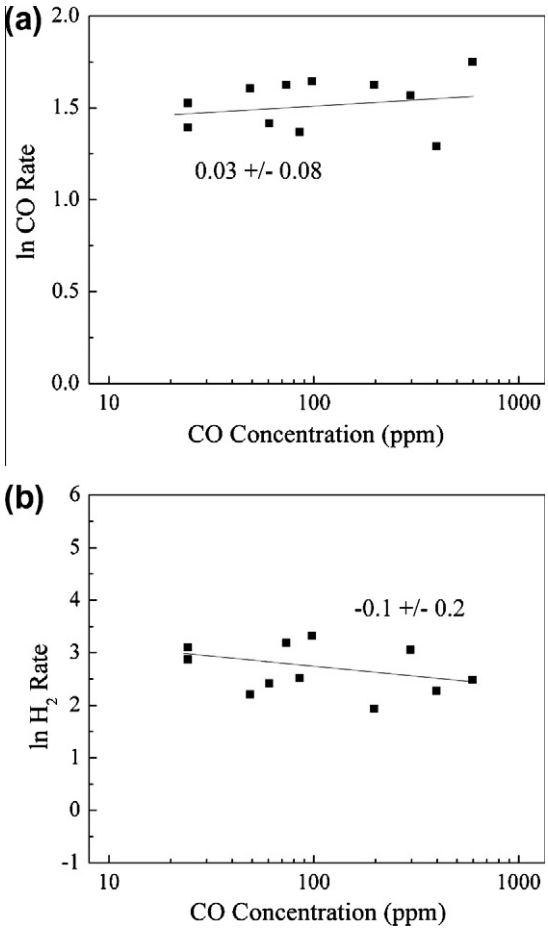

Fig. 5. Log–log plot of (a) CO oxidation rate and (b) H_2 oxidation rate as a function of CO concentration. Corresponding rates are given as 10^{-9} mol g^{-1} s^{-1}. Conditions: 25% H_2, 50 ppm O_2, bal He, T = 333 K.

In contrast to Fig. 4, Fig. 5 shows CO and H_2 oxidation rates as a function of CO concentration (20–1000 ppm) at much lower O_2 concentration (50 ppm). With only 50 ppm O_2, both CO and H_2 oxidation rates show zero order with respect to CO concentration and are considerably lower than with 0.5% O_2. The zero-order rate dependence on CO concentration suggests that even at low CO concentrations (20–400 ppm), the Pt surface is saturated with CO. In the case that the Pt surface is completely saturated with CO, it would be expected that the L–H rates for both CO and H_2 oxidation approach zero. According to the parallel pathway mechanism proposed in Section 3.3, if the L–H rate tends to zero, the total rate would then correspond to the M–vK pathway, in which the CO oxidation rate has a zero-order dependence on CO in the event that CO is the most abundant surface intermediate on the Pt sites (Eq. (24)). The H_2 oxidation rate must have a CO order between 0 and −1 (Eq. (25)) and is expected to be nearly zero order at very low O_2 pressures (50 ppm) where the surface is nearly saturated with CO and would not provide an inhibiting effect on the rate.

$$r_{CO} = \frac{z' k_{10} \sqrt{K_{11}[O_2]}[L][O^*]_T}{1 + \sqrt{K_{11}[O_2]} + K_8 \sqrt{K_5 K_{11}[O_2][H_2]}} \quad (24)$$

$$r_{H_2} = \frac{z' k_9 K_5 K_8 \sqrt{K_{11}[O_2]}[H_2][L][O^*]_T}{K_1[CO](1 + \sqrt{K_{11}[O_2]} + K_8 \sqrt{K_5 K_{11}[O_2][H_2]})} \quad (25)$$

From results presented in Figs. 4 and 5, it is apparent that CO coverage is the critical factor that determines which mechanistic pathway (L–H or M–vK) is dominant. CO coverage regimes seem to be driven by relative CO:O_2 concentrations. In Fig. 6, these regimes are demonstrated further by determining O_2 orders for low (25 ppm) and high (1%) concentrations of CO. In the low CO:O_2 concentration range, it would be expected that CO coverage is relatively low and that L–H kinetics would dominate. Eq. (18) predicts a positive partial order (between 0 and 1) with respect to O_2 when L–H kinetics dominate. Indeed, an O_2 reaction order of 0.58 is observed and shown in Fig. 6a. In the high CO:O_2 concentration range, CO is expected to dominate the surface with the M–vK pathway expected to control the rate. Eq. (19) predicts an O_2 order between 0 and 0.5 for M–vK controlled kinetics. An order of zero is observed and shown in Fig. 6b. The clear zero-order dependence on O_2 corresponds to conditions where all redox sites remain in a mostly oxidized state, as is typically observed for M–vK redox reactions [20].

CO and H_2 oxidation kinetics across this same range of relative CO and O_2 pressures was also investigated over the 0.41 Pt/CeO_2 catalyst to ensure that there was no mechanistic dependence on the crystalline state of the CeO_2 support. For this catalyst, a slightly lower temperature was investigated to retain differential reaction conditions, since rates were higher over this catalyst in comparison with the 0.43 Pt/CeO_2 catalyst. CO and H_2 oxidation rates and CO_2 selectivities are summarized in Table 2 and show identical orders and trends with CO and O_2 pressure as described previously with the 0.43 Pt/CeO_2 catalyst, confirming the presence of a dual L–H and M–vK reaction mechanism with a transition dependent on relative CO:O_2 pressure and causing dramatic selectivity loss under L–H conditions.

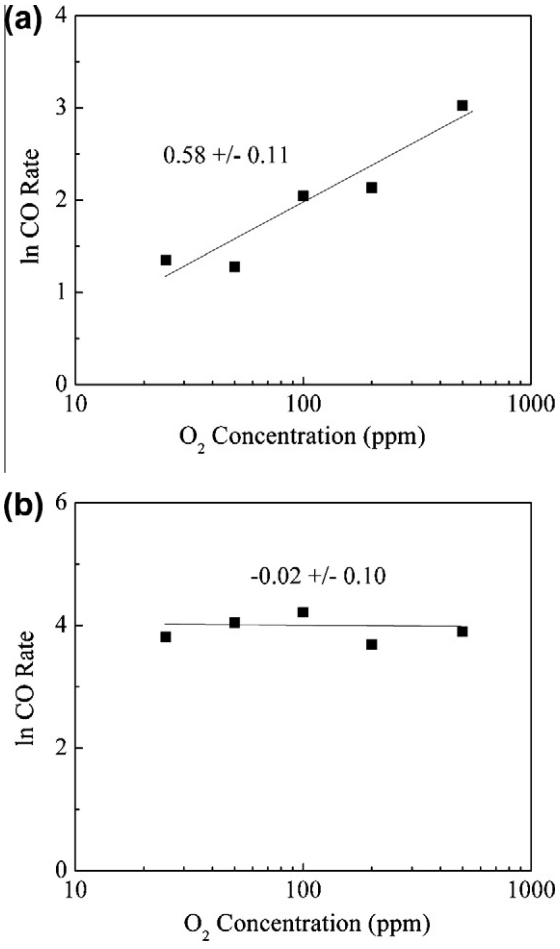

Fig. 6. Log–log plot of CO oxidation rate as a function of O_2 concentration at (a) 25 ppm CO, 25% H_2 and (b) 1% CO, 25% H_2. T = 333 K. Corresponding rates are given as 10^{-9} mol g^{-1} s^{-1}.

3.5. Redox site identification

An accurate quantification of redox sites is necessary to confirm the presence of the Mars and van Krevelen pathway and to confirm that active redox sites are at the interface of the Pt particles with CeO_2. The hypothesis that interfacial Pt–O–Ce sites are responsible for redox activity can be examined by investigating correlations between redox site density and Pt particle interfacial areas. Anaerobic titrations carried out under conditions controlled by M–vK kinetics can be used to quantify site densities of active lattice O^* (without inclusion of chemisorbed oxygen species). *In situ* DRIFTS experiments were conducted to ensure that Pt particles were mostly saturated with CO under conditions chosen for anaerobic experiments to minimize L–H pathways and oxidation rates. Fig. 7 shows the dependence of the amount of adsorbed CO (as interpreted by the peak area from ~1900 to 2100 cm^{-1}) on the concentration of CO during the oxidation of CO in 350 ppm O_2 on 2.78 Pt/CeO_2 at 333 K. CO peak areas during PROX reactions were compared to the CO peak area in the presence of only 650 ppm CO at 333 K (no oxygen present and the Pt surface is presumably saturated with CO). During reaction with 650 ppm CO and

Table 2
Oxidation kinetics over 0.41 wt% Pt/CeO_2 at 313 K (2.09 mg, 25% H_2, bal He) in both the Langmuir–Hinshelwood regime (0.5% O_2) and the Mars and van Krevelen regime (50 ppm O_2).

CO concentration (ppm)	O_2 concentration (ppm)	CO rate (mol × 10^{-9} g^{-1} s^{-1})	H_2 rate (mol × 10^{-9} g^{-1} s^{-1})	Selectivity (%)
50	5000	459	39,004	1
100	5000	896	14,960	6
200	5000	1091	4015	21
500	5000	941	553	63
700	5000	808	315	72
100	50	209	286	42
150	50	205	292	41
200	50	214	294	42

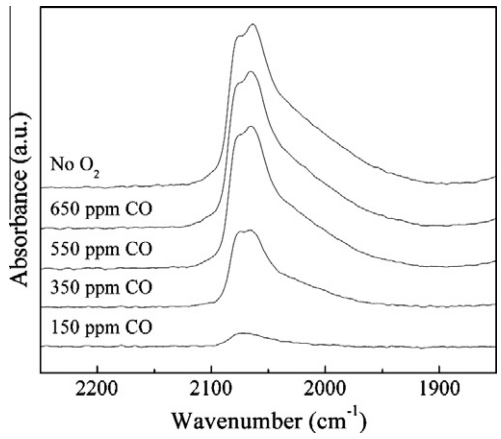

Fig. 7. DRIFTS spectra during CO oxidation (150–650 ppm) at 333 K over 2.78 Pt/CeO_2 in 350 ppm O_2. For the no O_2 experiment, the catalyst was exposed to 650 ppm CO balance He at 333 K for 15 min.

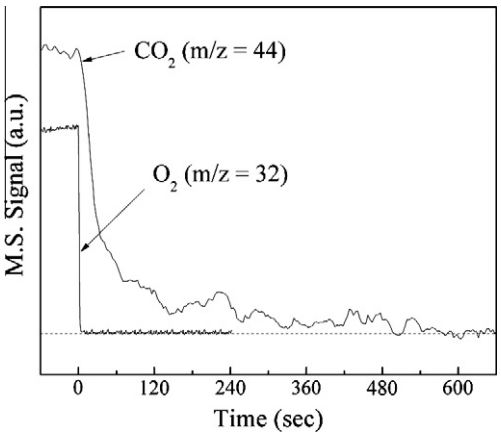

Fig. 9. Mass spectrometer response during anaerobic titration of 1.04 Pt/CeO_2 at 333 K. Initial conditions: 650 ppm CO, 350 ppm O_2, balance He. Horizontal dotted line indicates zero on the vertical scale.

350 ppm O_2, the Pt surface looks nearly identical to a surface saturated with CO. Thus, at these conditions, the surface contains minimal amounts of chemisorbed oxygen and anaerobic experiments at 650 ppm CO and 350 ppm O_2 will yield an accurate count of active redox sites.

Fig. 8 compares CO peak areas relative to the CO peak areas with 650 ppm CO in the absence of O_2, as a function of O_2 and CO concentration on 2.78 Pt/CeO_2. Relative peak areas are considerably higher in the presence of 350 ppm O_2 than at 3% O_2, especially at 650 ppm CO (0.91 and 0.18, respectively). Clearly, in the presence of 3% O_2, the CO coverage on Pt is low and Langmuir–Hinshelwood reaction rates would be quite high and dominant in this CO concentration range. The effects of CO and O_2 concentrations on relative CO coverage are another indicator that the CO/O_2 concentration ratio is very important in determining the kinetic regime for Pt/CeO_2 catalysts.

The mechanism proposed in Section 3.3 implies that the oxygen used for the redox pathway is adjacent to metal sites. If interfacial Pt–O–Ce sites are responsible for the redox pathway, the number of sites should correlate with the interfacial contact length of the Pt particles on the CeO_2 support, or rates normalized by the amount of interfacial Pt–O–Ce sites should be constant regardless of Pt loading or dispersion. In order to count the redox sites on the Pt/CeO_2 catalyst series, anaerobic titrations were utilized [27]. In this technique, O_2 is instantaneously replaced with inert gas (He) during a steady-state oxidation reaction. During a M–vK redox reaction, lattice oxygen is used to oxidize CO to CO_2 and in the absence of gas-phase O_2, such sites are stoichiometrically titrated. Integration of the decaying rate of product formation with time provides a measure of the total number of titrated redox sites.

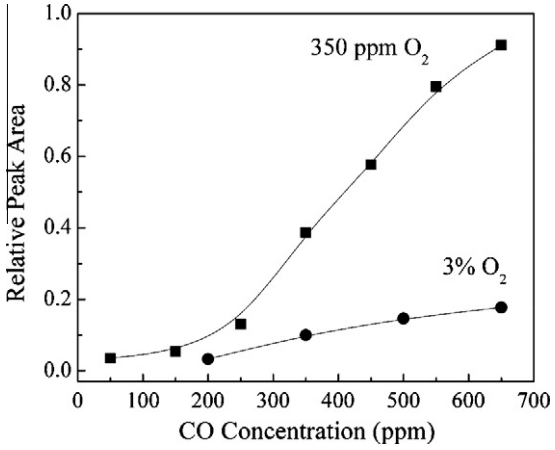

Fig. 8. Effect of O_2 concentration on relative peak area during CO oxidation on 2.78 Pt/CeO_2 at 333 K (350 ppm O_2 (■); 3% O_2 (●)).

Fig. 9 shows CO anaerobic titration over 1.04 Pt/CeO_2 at 333 K during reaction with 650 ppm CO and initially 350 ppm CO during the initial steady-state reaction (confirmed M–vK regime). The effluent O_2 signal drops to zero within ~5 s, while the oxidation product (CO_2) decays over ~600 s. The curve is integrated to yield an amount of redox sites (O^*) per gram of catalyst.

Table 3 shows the measured molar redox site densities at 333 K over 4 investigated Pt/CeO_2 catalysts normalized per g catalyst, per mol Pt, per mol exposed Pt, and relative densities normalized per mol interfacial Pt (neighboring CeO_2). Over 0.41, 1.04 and 2.78 Pt/CeO_2 prepared on a common CeO_2 support with similar surface area (Table 1), the density of active redox sites per interfacial length is nearly constant (within a factor of about 2, versus an order of magnitude differences in O^* density per m^2 of catalyst surface), implying that active redox sites are associated with interfacial Pt–O–Ce bonds. Therefore, M–vK rates per Pt over Pt/CeO_2 catalysts are dependent on the amount of interfacial area available between the Pt particles and the support. O^* densities per exposed Pt atom, however, are greater than 1 over these three catalysts, indicating that although oxygen must pass through a Pt–O–Ce interfacial site during redox reactions with CO or H_2, oxygen at these sites can be replenished by the bulk CeO_2 support (not in contact with Pt) during the anaerobic titration experiments. Further studies will be required to identify whether or not oxygen migration also occurs during steady-state reactions at constant oxygen pressure. The 0.43 Pt/CeO_2 catalyst has a molar redox site concentration per Pt about 30–40 times lower than the other catalysts. The molar O^* density per mol exposed Pt is only 0.2. The fractional value (lower than 1) indicates that the bulk CeO_2 support used in this catalyst (and not in contact with Pt) is much less reducible as a result of its higher crystallinity (Table 1); it does not provide additional oxygen species during redox reactions with CO or H_2. High CeO_2 support crystallinity has previously been related to a lower redox activity [10].

3.6. Conditions governing reaction selectivity

As shown in Section 3.2, Pt/CeO_2 catalysts have potential for highly selective behavior under certain conditions but have exhibited large selectivity losses when subjected to conditions that

Table 3
Redox site densities (O^*) of Pt/CeO_2 catalysts at 333 K.

Catalyst name	Mol O^*/g catalyst	Mol O^*/mol Pt	Mol O^*/mol exposed Pt	Relative Mol O^*/mol interfacial Pt[a]
0.43 Pt/CeO_2	2.0×10^{-6}	0.1	0.2	0.04
0.41 Pt/CeO_2	6.9×10^{-5}	3.3	4.0	0.75
1.04 Pt/CeO_2	2.0×10^{-4}	3.8	4.9	1.00
2.78 Pt/CeO_2	5.8×10^{-4}	4.1	6.7	1.68

[a] Calculated by multiplying Mol O^*/mol exposed Pt by the Pt particle diameter (estimated at 1.2–1.6 nm), which is used as a geometric shape factor for area/length and represents the ratio of exposed Pt atoms on a hemisphere to the number of exposed Pt atoms along the circumference of the hemisphere in contact with the CeO_2 support (relative values were obtained by normalizing to the 1.04 Pt/CeO_2 site density per length).

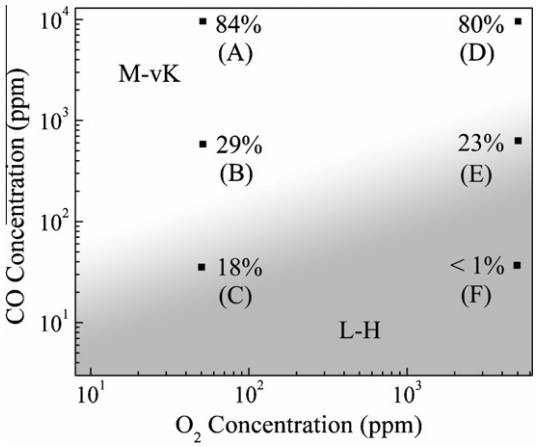

Fig. 10. CO_2 selectivity (next to markers) at different $CO:O_2$ conditions at 333 K and 25% H_2 on 0.43 Pt/CeO_2. Selectivities reported are under differential conditions (X_{CO}, $X_{O2} < 10\%$). Mars and van Krevelen (M–vK) and Langmuir–Hinshelwood (L–H) regimes are shown by shading. CO and H_2 Oxidation rates in 10^{-8} mol g^{-1} s^{-1}, respectively, for each point A–F are: (A) 5.70, 1.05; (B) 0.57, 1.20; (C) 0.43, 1.99; (D) 5.64, 1.38; (E) 9.40, 31.81; (F) 16.67, 2899.

result in low CO coverage of Pt. Fig. 10 shows reaction selectivity (under differential conditions) as a function of both CO and O_2 concentration at 25% H_2 and 333 K. Also shown in Fig. 10 is the differentiation between Mars and van Krevelen (M–vK) and Langmuir–Hinshelwood (L–H) kinetically controlled regimes. CO and H_2 oxidation rates at these conditions are also summarized in the caption of Fig. 10. The gradient (transition) region in Fig. 10 is an approximation of where $r_{CO,L-H} \approx r_{CO,M-vK}$. Lowering the CO concentration from points at either 50 ppm O_2/25 ppm CO (C) or 5000 ppm O_2/600 ppm CO (E) results in a distinct increase in H_2 oxidation rates much like in Fig. 4b. For example, at point E, r_{H2} changes from 3.2×10^{-7} to 2.9×10^{-5} mol g^{-1} s^{-1} when CO concentration is lowered to 25 ppm (Point F). Both CO and H_2 oxidation rates are generally higher when operating in the L–H regime (5.7×10^{-8} and 1.1×10^{-8} mol g^{-1} s^{-1} for CO and H_2 oxidation rates, respectively, at point A versus 1.7×10^{-7} and 2.9×10^{-5} mol g^{-1} s^{-1} at point F), with H_2 rates substantially higher than CO rates in the L–H regime and leading to marked losses in selectivity. Therefore, the M–vK pathway is considerably more selective on Pt/CeO_2. A purely M–vK pathway has a selectivity of 84% and a purely L–H pathway has a selectivity below 1%. Also, the selectivity is generally intermediate when close to the boundary between the two regimes.

4. Conclusions

A detailed study of CO and H_2 oxidation over a series of Pt/CeO_2 catalysts with varying Pt weight loadings and dispersions was conducted, and the following major conclusions can be made.

- Both CO and H_2 oxidation occur by parallel Langmuir–Hinshelwood and Mars and van Krevelen mechanistic pathways. At low CO coverage, Langmuir–Hinshelwood kinetics dominates, while at high CO coverage the Mars and van Krevelen pathway dominates the rate.
- Selectivity losses at low CO concentrations result from a low CO coverage on Pt leading to conditions dominated by a Langmuir–Hinshelwood pathway. Under these conditions, H_2 oxidation rates on Pt are considerable.
- CO coverage is primarily controlled by relative concentrations of CO and O_2.
- Redox site concentrations can be measured by anaerobic titrations under conditions where M–vK kinetics dominate the rate. A constant redox site density per interfacial Pt length over catalysts with similar CeO_2 supports shows the importance of interfacial Pt–O–Ce sites for redox activity.

Acknowledgments

Funding was provided by Purdue University and the Purdue Research Foundation. The authors acknowledge Ms. Carrie Clark for contributions to catalyst testing. Use of the Advanced Photon Source is supported by the US Department of Energy, Office of Science and Office of Basic Energy Sciences, under Contract DE-AC02-06CH11357. MRCAT operations are supported by the Department of Energy and the MRCAT member institutions.

References

[1] F. Arena, P. Famulari, G. Trunfio, G. Bonura, F. Frusteri, L. Spadaro, Applied Catalysis B: Environmental 66 (2006) 81.
[2] W. Deng, J.D. Jesus, H. Saltsburg, M. Flytzani-Stephanopoulos, Applied Catalysis A: General 291 (2005) 126.
[3] G. Panzera, V. Modafferi, S. Candamano, A. Donato, F. Frusteri, P.L. Antonucci, Journal of Power Sources 135 (2004) 177.
[4] X. Tang, B. Zhang, Y. Li, Y. Xu, Q. Xin, W. Shen, Catalysis Letters 97 (2004) 163.
[5] O. Pozdnyakova, D. Teschner, A. Wootsch, J. Krohnert, B. Steinhauer, H. Sauer, L. Toth, F.C. Jentoft, A. Knop-Gericke, Z. Paal, R. Schlogl, Journal of Catalysis 237 (2006) 1.
[6] O. Pozdnyakova-Tellinger, D. Teschner, J. Krohnert, F.C. Jentoft, A. Knop-Gericke, R. Schlogl, A. Wootsch, Journal of Physical Chemistry C 111 (2007) 5426.
[7] C. Pedrero, T. Waku, E. Iglesia, Journal of Catalysis 233 (2005) 242.
[8] M.M. Schubert, M.J. Kahlich, H.A. Gasteiger, R.J. Behm, Journal of Power Sources 84 (1999) 175.
[9] G.S. Zafiris, R.J.U.o.P. Gorte, Philadelphia, PA (United States), Journal of Catalysis, vol. 143 (1), DOE Project (1993), p. 86.
[10] T. Bunluesin, R.J. Gorte, G.W. Graham, Applied Catalysis B: Environmental 14 (1997) 105.
[11] S.Y. Chin, O.S. Alexeev, M.D. Amiridis, Journal of Catalysis 243 (2006) 329.
[12] G. Avgouropoulos, T. Ioannides, H.K. Matralis, J. Batista, S. Hocevar, Catalysis Letters 73 (2001) 33.
[13] D. Gamarra, G. Munuera, A.B. Hungria, M. Fernandez-Garcia, J.C. Conesa, P.A. Midgley, X.Q. Wang, J.C. Hanson, J.A. Rodriguez, A. Martinez-Arias, Journal of Physical Chemistry C 111 (2007) 11026.
[14] Y. Liu, Q. Fu, M. Flytzani-Stephanopoulos, Catalysis Today 93–95 (2004) 241.
[15] G. Marban, A.B. Fuertes, Applied Catalysis B: Environmental 57 (2005) 43.
[16] C.S. Polster, C.D. Baertsch, Chemical Communications (2008) 4046.
[17] G. Sedmak, S. Hocevar, J. Levec, Journal of Catalysis 213 (2003) 135.

[18] A. Martinez-Arias, A.B. Hungria, M. Fernandez-Garcia, J.C. Conesa, G. Munuera, Journal of Physical Chemistry B 108 (2004) 17983.
[19] X. Wang, I.E. Wachs, Catalysis today selective catalytic oxidation: fundamentals, in: Application and Environmental Impacts – ACS National Meeting, New York, 7–11 September 2003, vol. 96, 2004, p. 211.
[20] W. Liu, M. Flytzani-Stephanopoulos, Journal of Catalysis 153 (1995) 317.
[21] C. Lamonier, A. Ponchel, A. D'Huysser, L. Jalowiecki-Duhamel, Catalysis Today 50 (1999) 247.
[22] S. Derrouiche, D. Bianchi, Journal of Catalysis 230 (2005) 359.
[23] O. Pozdnyakova, D. Teschner, A. Wootsch, J. Kröhnert, B. Steinhauer, H. Sauer, L. Toth, F.C. Jentoft, A. Knop-Gericke, Z. Paál, R. Schlögl, Journal of Catalysis 237 (2006) 17.
[24] G. Avgouropoulos, T. Ioannides, Applied Catalysis B: Environmental 67 (2006) 1.
[25] S. Zhou, Z. Yuan, S. Wang, International Journal of Hydrogen Energy 31 (2006) 924.
[26] E. Moretti, M. Lenarda, L. Storaro, A. Talon, R. Frattini, S. Polizzi, E. Rodriguez-Castellon, A. Jimenez-Lopez, Applied Catalysis B: Environmental 72 (2007) 149.
[27] H. Nair, C.D. Baertsch, Journal of Catalysis 258 (2008) 1.
[28] B. Frank, R. Fortrie, C. Hess, R. Schlögl, R. Schomäcker, Applied Catalysis A: General 353 (2009) 288.
[29] J.T. Miller, A.J. Kropf, Y. Zha, J.R. Regalbuto, L. Louis Delannoy, E. Bus, J.A. Bokhoven, Journal of Catalysis 240 (2006) 222–234.